Structural and Biochemical Basis for Development of Influenza Virus Inhibitors Targeting the PA Endonuclease

Rebecca M. DuBois[1,2], P. Jake Slavish[3], Brandi M. Baughman[3,4], Mi-Kyung Yun[1], Ju Bao[1], Richard J. Webby[2], Thomas R. Webb[3,4], Stephen W. White[1,4]*

1 Department of Structural Biology, St. Jude Children's Research Hospital, Memphis, Tennessee, United States of America, 2 Department of Infectious Diseases, St. Jude Children's Research Hospital, Memphis, Tennessee, United States of America, 3 Department of Chemical Biology and Therapeutics, St. Jude Children's Research Hospital, Memphis, Tennessee, United States of America, 4 Integrated Program in Biomedical Sciences, University of Tennessee Health Science Center, Memphis, Tennessee, United States of America

Abstract

Emerging influenza viruses are a serious threat to human health because of their pandemic potential. A promising target for the development of novel anti-influenza therapeutics is the PA protein, whose endonuclease activity is essential for viral replication. Translation of viral mRNAs by the host ribosome requires mRNA capping for recognition and binding, and the necessary mRNA caps are cleaved or "snatched" from host pre-mRNAs by the PA endonuclease. The structure-based development of inhibitors that target PA endonuclease is now possible with the recent crystal structure of the PA catalytic domain. In this study, we sought to understand the molecular mechanism of inhibition by several compounds that are known or predicted to block endonuclease-dependent polymerase activity. Using an in vitro endonuclease activity assay, we show that these compounds block the enzymatic activity of the isolated PA endonuclease domain. Using X-ray crystallography, we show how these inhibitors coordinate the two-metal endonuclease active site and engage the active site residues. Two structures also reveal an induced-fit mode of inhibitor binding. The structures allow a molecular understanding of the structure-activity relationship of several known influenza inhibitors and the mechanism of drug resistance by a PA mutation. Taken together, our data reveal new strategies for structure-based design and optimization of PA endonuclease inhibitors.

Introduction

Influenza viruses can cause sporadic global pandemics, and they can result in high mortality rates such as the 1918 pandemic that resulted in 30 to 50 million deaths worldwide [1]. The recent 2009 pandemic was caused by a novel H1N1 virus that originated in swine [2], but of more concern is the impending threat of the highly pathogenic avian influenza H5N1 viruses that cause mortality rates approaching 60% when transmitted to humans [3]. Although H5N1 viruses have yet to naturally acquire the capacity for efficient human-to-human transmission, this has recently been demonstrated in animal models [4,5] and they remain an ever-present threat due to their continued circulation in avian species. The development of a new vaccine requires several months, and effective antiviral therapies are therefore important at the beginning of a fast-spreading pandemic. Antivirals that target the M2 ion channel (amantadine and rimantadine) or neuraminidase (zanamivir and oseltamivir) have proven to be effective at reducing the severity of illness (reviewed in [6]), but the rapid emergence of resistant strains has highlighted the need for new therapeutic options [7].

Influenza virus contains a negative-strand segmented RNA genome comprising eight ribonucleoprotein assemblies. The RNA-dependent RNA polymerase (RdRp) catalyzes both the transcription and replication steps that are essential in the virus life cycle. The RdRp is a heterotrimeric complex comprising subunits PA, PB1, and PB2 that associates with the 3′ and 5′ ends of each RNA genome segment [8,9]. Translation of viral mRNAs by the host ribosome requires 5′ capping, and the necessary mRNA caps are cleaved or "snatched" from host pre-mRNAs. This "cap-snatching" mechanism begins with the binding of PB2 to the cap of a host pre-mRNA, followed by the cleavage of the pre-mRNA by the endonuclease functionality [10,11,12]. The resulting 10- to 14-residue cap-containing oligonucleotide is then used as a primer for viral mRNA transcription by PB1 [13,14].

The endonuclease activity is an excellent target for the development of new anti-influenza inhibitors [15], and recent crystallographic studies have facilitated this approach. Two groups found that the endonuclease activity resides not in PB1 as previously suggested [11] but in an independently folded N-terminal domain of PA (PA$_N$) [16,17]. This explains previous findings that PA-specific siRNA can down-regulate viral mRNA

Author Summary

Seasonal and pandemic influenza have enormous impacts on global public health. The rapid emergence of influenza virus strains that are resistant to current antiviral therapies highlights the urgent need to develop new therapeutic options. A promising target for drug discovery is the influenza virus PA protein, whose endonuclease enzymatic activity is essential for the "cap-snatching" step of viral mRNA transcription that allows transcripts to be processed by the host ribosome. Here, we describe a structure-based analysis of the mechanism of inhibition of the influenza virus PA endonuclease by small molecules. Our X-ray crystallographic studies have resolved the modes of binding of known and predicted inhibitors, and revealed that they directly block the PA endonuclease active site. We also report a number of molecular interactions that contribute to binding affinity and specificity. Our structural results are supported by biochemical analyses of the inhibition of enzymatic activity and computational docking experiments. Overall, our data reveal exciting strategies for the design and optimization of novel influenza virus inhibitors that target the PA protein.

production and block virus replication in cell culture [18]. The crystal structures revealed that PA_N is a member of the PD-(D/E)XK nuclease superfamily, although there was disagreement as to whether there is a single magnesium (Mg^{2+}) ion in the active site [17] or two manganese (Mn^{2+}) ions [16]. However, PA_N has greater thermal stability and higher endonuclease activity in the presence of Mn^{2+} ions than other divalent cations [16], and isothermal titration calorimetry (ITC) [19] and earlier studies [20] also support the presence of two Mn^{2+} ions.

During the past 5 years, structural studies have revealed that the influenza RdRp comprises multiple, independently-folded, sub-domains with defined functionalities, and the PA_N domain structure is particularly important with implications for structure-based drug discovery [10,16,17,21,22,23,24,25]. Mutational analyses support the idea that the PA_N domain is a valuable vehicle for drug discovery [12,17,19]. Previous studies have reported inhibitors of influenza transcription and/or endonuclease activity, but there are no structural data demonstrating their molecular mechanisms [15,26,27,28,29,30]. Here, we present crystal structures of PA_N from strain A/Vietnam/1203/2004 (H5N1) in complex with six known or predicted inhibitors that allow us to precisely describe their interactions with the PA_N active site. In an accompanying article by Kowalinski and coworkers, structures of a complementary set of inhibitors in complex with PA_N from strain A/California/04/2009 (H1N1) are reported [31]. Together, our structures provide a molecular explanation for the structure-activity relationship (SAR) of several related influenza inhibitors, reveal the mechanism of drug-resistance by a PA mutation, and provide a solid basis for future structure-based drug discovery efforts.

Results

Structural Analysis of a Modified PA_N Domain

The structure of the PA_N domain has been reported in two studies [16,17], but neither construct was considered suitable for drug discovery. In one structure, a 22-residue loop of one PA_N molecule packs into the active site of a neighboring molecule [16] making it unavailable for inhibitor binding. In the second structure, although these loop residues are disordered and the

PA_N active site is suitably exposed, we were unable to reproduce these crystals at high resolution [17]. We therefore designed a new truncated construct of PA_N, termed $PA_N^{\Delta Loop}$, from strain A/Vietnam/1203/2004 (H5N1) (Fig. 1A), in which the loop is replaced by a Gly-Gly-Ser linker and which ends at residue 196, the last visible residue in both of the crystal structures. $PA_N^{\Delta Loop}$ readily crystallized in a new crystal form that diffracted to 2.05 Å (Table 1, $PA_N^{\Delta Loop}$–Apo) with four molecules in the asymmetric unit and all active sites exposed (Fig. S1A). The $PA_N^{\Delta Loop}$ structure is essentially identical to the previously reported structures of PA_N (backbone alpha-carbon RMSD of 0.45 Å). Importantly, the active site residues are virtually superimposable (Fig. 1B), two metal ions are clearly present (Fig. 1B), and the dose-dependent endonuclease activity is unaffected by the truncations (Fig. 1C, 1D). This suggests that the function of the loop is architectural rather than catalytic, presumably to mediate interactions with another subunit of the influenza RdRp or with a host cell factor.
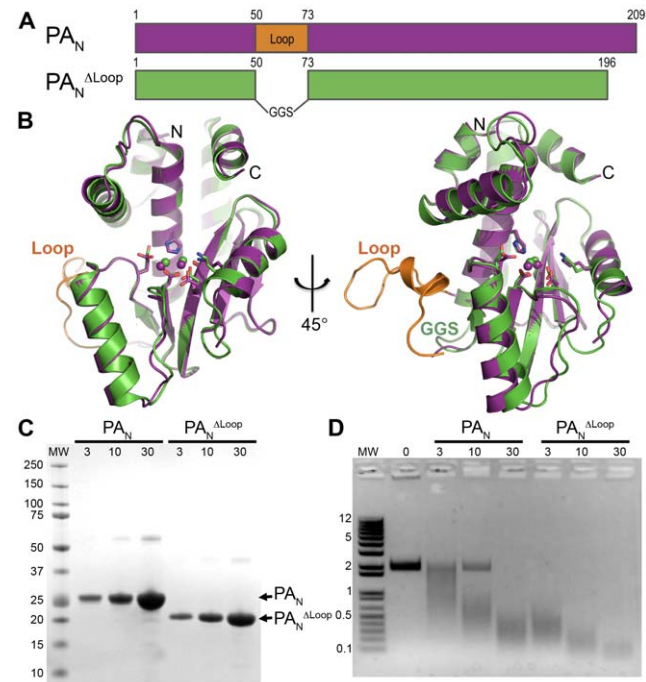

Figure 1. Crystal structure and endonuclease activity of $PA_N^{\Delta Loop}$. (**A**) Schematic of PA_N (magenta) and $PA_N^{\Delta Loop}$ (green), and location of the 22-residue loop (orange) replaced by a Gly-Gly-Ser linker in the $PA_N^{\Delta Loop}$ construct. (**B**) Two orthogonal views of the overlay of the crystal structures of PA_N and $PA_N^{\Delta Loop}$, colored as in **A**. Key active site residues are shown in stick representation, the paired manganese ions are shown as spheres, and the N- and C-termini are labeled. The coordinates for PA_N are from PDB entry 2W69. The atomic coordinates and structure factors for $PA_N^{\Delta Loop}$ have been deposited in the Protein Data Bank as PDB entry 4E5E. (**C**) Coomassie-stained SDS-PAGE of PA_N and $PA_N^{\Delta Loop}$ showing the amount of protein (μM) in a 10 μl endonuclease activity assay reaction. Molecular weight (MW) markers (kD) are shown on the left. (**D**) Endonuclease activity assay with PA_N and $PA_N^{\Delta Loop}$. Single-stranded DNA plasmid M13mp18 was incubated with increasing concentrations (μM) of PA_N or $PA_N^{\Delta Loop}$. Reactions products were resolved on a 1.0% agarose gel stained with ethidium bromide. Molecular weight (MW) ladder (kb) is shown on the left.
doi:10.1371/journal.ppat.1002830.g001

Table 1. Crystallographic statistics.

Data collection[a]

Crystal	PA$_N$-Apo	PA$_N$-compound 1	PA$_N$-compound 2	PA$_N$-compound 3	PA$_N$-compound 4	PA$_N$-compound 5	PA$_N$-compound 6
Space group	C222$_1$	C222$_1$	C222$_1$	C222$_1$	C222$_1$	C222$_1$	C222$_1$
a, b, c (Å)	126.4, 133.9, 126.4	126.6, 134.3, 126.7	126.9, 133.7, 126.8	126.1, 134.8, 125.9	126.3, 134.8, 126.5	126.1, 134.1, 126.6	126.5, 133.5, 126.4
α, β, γ (°)	90.0, 90.0, 90.0	90.0, 90.0, 90.0	90.0, 90.0, 90.0	90.0, 90.0, 90.0	90.0, 90.0, 90.0	90.0, 90.0, 90.0	90.0, 90.0, 90.0
Resolution (Å)	50.0–2.05 (2.12–2.05)	50.0–2.40 (2.49–2.40)	50.0–2.65 (2.74–2.65)	50.0–2.15 (2.23–2.15)	50.0–2.95 (3.06–2.95)	50.0–2.35 (2.43–2.35)	50.0–2.50 (2.59–2.50)
R_{merge}	0.063 (0.457)	0.072 (0.488)	0.072 (0.495)	0.065 (0.511)	0.071 (0.488)	0.073 (0.484)	0.081 (0.528)
$I/\sigma I$	31.0 (3.0)	35.3 (4.5)	36.9 (5.2)	27.3 (4.3)	28.7 (2.2)	32.4 (5.9)	37.1 (4.7)
Completeness (%)	99.6 (96.3)	99.9 (100.0)	99.9 (99.9)	99.8 (100.0)	96.6 (74.4)	99.8 (100.0)	99.9 (100.0)
Redundancy	8.0 (5.7)	10.3 (9.5)	12.4 (12.0)	9.0 (7.4)	8.4 (5.3)	12.0 (11.3)	10.3 (9.6)
Refinement							
Resolution (Å)	50.0–2.05	50.0–2.40	50.0–2.65	50.0–2.15	50.0–2.95	50.0–2.35	50.0–2.50
No. reflections	88,796	56,039	41,126	76,756	29,768	58,174	52,052
R_{work}/R_{free}[b]	0.226/0.260	0.242/0.288	0.244/0.285	0.251/0.285	0.320/0.368	0.250/0.290	0.239/0.288
Ramachandran (%)							
Favored	98.7	98.3	98.5	98.6	96.9	98.2	98.7
Allowed	1.3	1.7	1.5	1.4	3.1	1.8	1.3
Outliers	0.0	0.0	0.0	0.0	0.0	0.0	0.0
Rms deviations							
Bond lengths (Å)	0.008	0.010	0.008	0.011	0.006	0.010	0.011
Bond angles (Å)	0.992	1.148	1.063	1.156	0.877	1.164	1.169

[a]Data were collected from a single crystal. Values for the highest-resolution shell are shown in parentheses.
[b]R_{free} was calculated using 5% of the reflections.
doi:10.1371/journal.ppat.1002830.t001

Metal Ion Binding in the PA$_N$ Active Site

Previous structural studies raised the question as to whether there is a single Mg^{2+} ion [17] or two Mn^{2+} ions [16] in the PA$_N$ active site. Because of this uncertainty, we included both 10 mM MgCl$_2$ and 5 mM MnCl$_2$ in our crystal soaking solutions. We eventually modeled two Mn^{2+} ions into the active sites of all of our structures for the following reasons. First, PA$_N^{\Delta Loop}$–Apo crystals soaked in a solution containing only 5 mM MnCl$_2$ revealed strong electron density in both metal sites (Fig. S1B). Second, refinements of all our structures consistently favored Mn^{2+} over Mg^{2+} ions to account for the observed electron densities. Third, ITC studies have shown that two Mn^{2+} ions bind tighter than one Mg^{2+} ion [19]. Finally, in the accompanying article by Kowalinski and coworkers, a strong anomalous signal for Mn^{2+} was observed in both metal sites when diketo inhibitors or mononucleotides are bound to PA$_N$ [31].

Inhibition of PA$_N$ Endonuclease Activity by Three Known Polymerase Inhibitors

We first investigated three known inhibitors of the influenza RdRp, compounds 1–3 (Fig. 2). Compound 1 is an *N*-hydroxyimide that has been shown to inhibit transcription *in vitro* [29], and it is structurally related to Flutimide that was found to specifically inhibit transcription, endonuclease activity, and influenza virus replication [30]. Compounds 2 (2,4-dioxo-4-phenylbutanoic acid, or DPBA) and 3 (L-742,001) are members of a series of 4-substituted 2,4-dioxobutanoic acids that were found to inhibit both transcription and endonuclease activities by purified RdRp *in vitro* [15]. Compound 3 is one of the most potent inhibitors of influenza transcription, and it exhibits dose-dependent inhibition of viral

replication in cell culture (IC$_{50}$ value 0.35 µM) and in mice [15,26]. Purified, recombinant PA$_N$ was incubated with single-stranded DNA substrate and increasing concentrations of 1, 2, and 3 (Fig. 3), and each inhibited PA$_N$ enzymatic activity in a dose-dependent manner. While this activity has been reported for 2 [16], this is the first evidence that 1 and 3 also inhibit the isolated PA$_N$ domain.

To investigate the mechanisms of action of 1, 2, and 3, we determined their co-crystal structures with PA$_N^{\Delta Loop}$ (Table 1). Clear difference electron density showed each compound adjacent to the active site Mn^{2+} ions (Figs. 4, S2). In each structure, the three adjacent and planar oxygen atoms on the inhibitor chelate the two Mn^{2+} ions in a pairwise fashion such that the central oxygen atom is shared by the ions. Thus, Mn^{2+} ion 1 (Mn1) is octahedrally coordinated to His41, Asp108, Glu119, Ile120 (carbonyl) and two oxygen atoms in the inhibitor, and Mn2 is tetrahedrally coordinated by Glu80, Asp108, and two oxygen atoms in the inhibitor. The side oxygen atom of the former pair also forms hydrogen bonds to Lys134, a key catalytic residue [12,16,17,19], and an ordered water molecule (H$_2$O^{122}).

The orientation of compound 1 in the active site was not entirely clear. Two of the four molecules in the asymmetric unit showed convincing electron density for the orientation shown in Figures 4A and S2A, while the orientations of the other two molecules were ambiguous. This ambiguity may reflect the weak electron density, possibly due to the poor solubility of 1 in the crystal soak solution. Alternatively, the benzene ring forms no obvious interactions with PA$_N^{\Delta Loop}$, and 1 may be free to adopt two alternate docking modes.

Compound 2 has also been structurally characterized in complex with the La Crosse virus endonuclease, and it engages
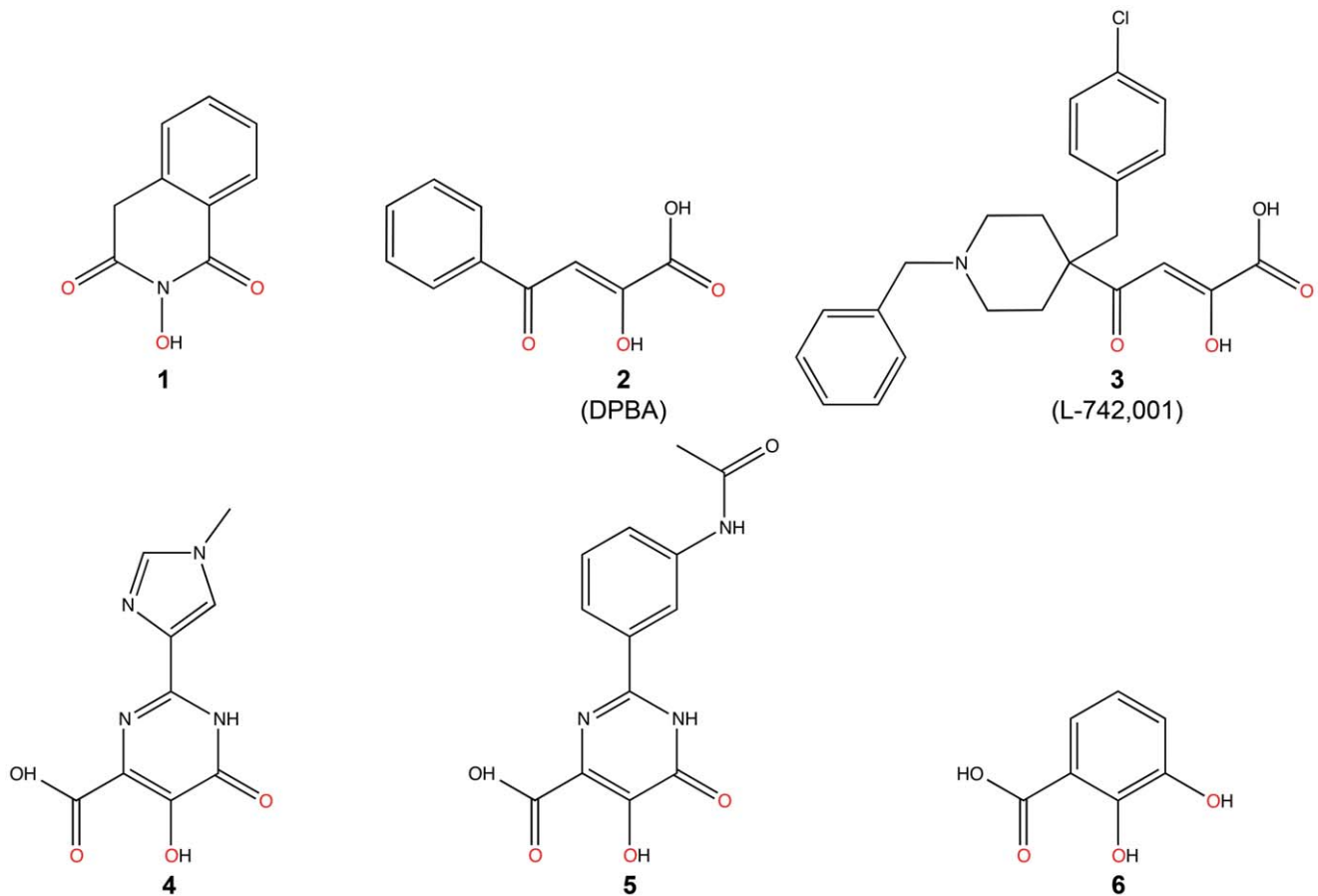
Figure 2. Chemical structures of compounds used in this study. Oxygen atoms that coordinate manganese ions in the active site of $PA_N^{\Delta Loop}$ are colored red.
doi:10.1371/journal.ppat.1002830.g002

the two-metal active site in the same fashion [32]. However, in the PA_N complex, two copies of the molecule are bound in the active site. Molecule A engages the Mn^{2+} ions and molecule B π-stacks onto molecule A in a parallel fashion via the phenyl group and the planar side chain (Figs. 4, S2). This arrangement was present in all four active sites in the asymmetric unit. The carboxyl group of molecule A forms a salt bridge to Lys134 and hydrogen bonds to metal-coordinating residues His41, Glu119, and Ile120 (carbonyl) and to H_2O^{122}. Molecule B engages a pocket comprising Ala20,

Met21, Glu26, Lys34, and Ile38 (Figs. 4B), and its carboxyl side chain also forms hydrogen bonds to His41 and H_2O^{122} in a fashion similar to that of molecule A. The phenyl groups of both molecules form an edge-to-face interaction with the side chain of Tyr24 that is pushed out approximately 2.0 Å in comparison with the $PA_N^{\Delta Loop}$-Apo structure. This suggests that the binding of compound **2** involves an induced-fit mechanism (Figs. 4, S3), and the relatively high B-factors in helix-α3 that contains Tyr24 reveal that this region is suitably mobile (Fig. S3).

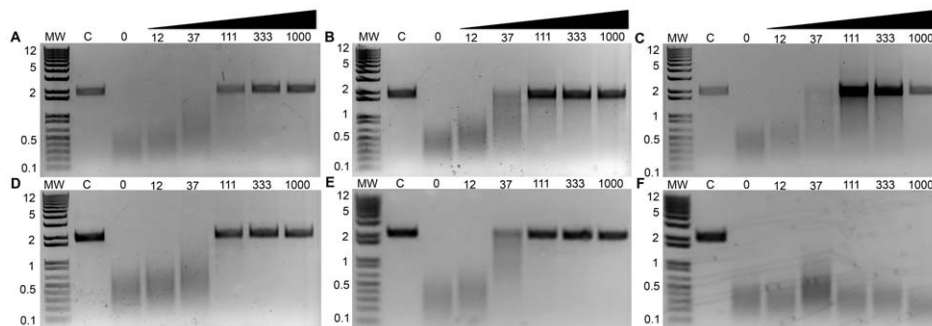**Figure 3. Inhibition of PA_N endonuclease activity by known and predicted inhibitors.** Compounds **1–6** (**A–F**, respectively) were incubated at increasing concentrations (μM) with 15 μM PA_N and single-stranded DNA plasmid M13mp18. Reaction products were resolved on a 1.0% agarose gel and stained with ethidium bromide. Control lanes ('C') contained no PA_N in the reaction mixture. Molecular weight (MW) ladder (kb) is shown on the left.
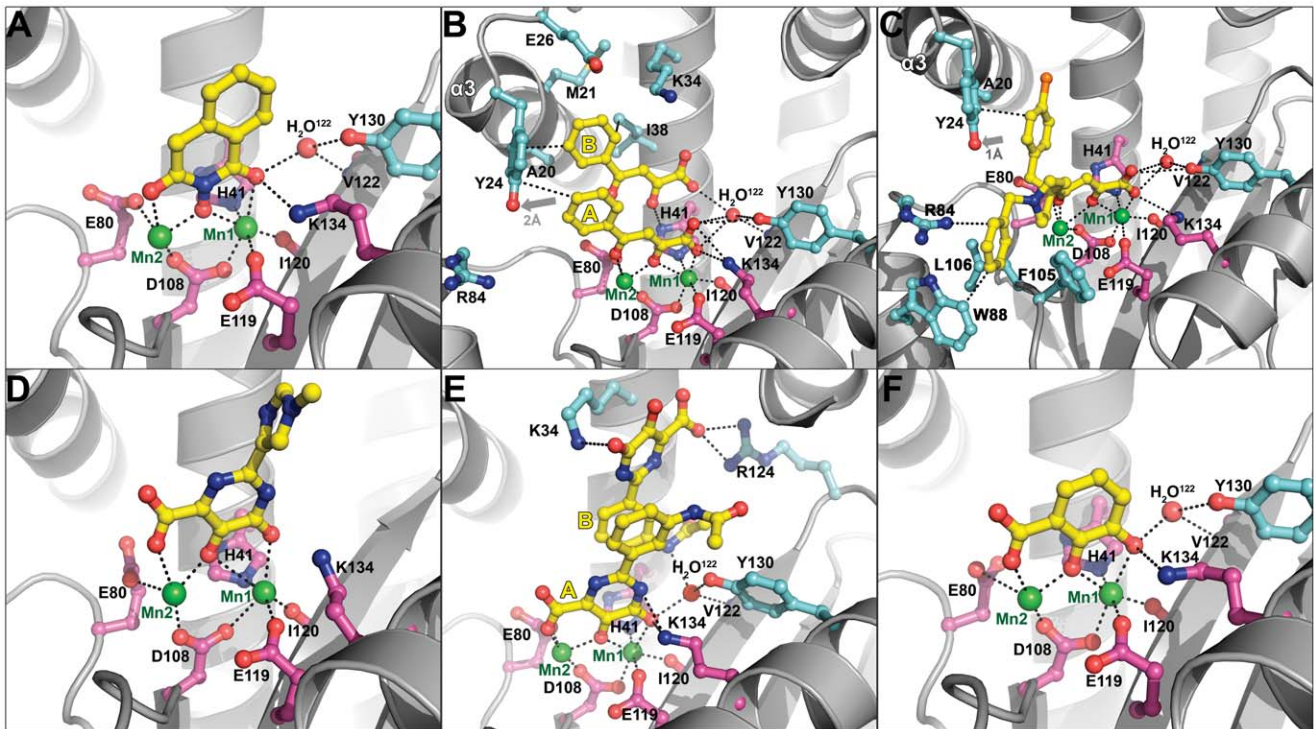doi:10.1371/journal.ppat.1002830.g003

Figure 4. Crystal structures of PA$_N^{\Delta Loop}$ bound to compounds 1–6 (A–F, respectively). PA$_N^{\Delta Loop}$ is shown as gray cartoon. Compounds are shown as ball-and-stick models and are colored yellow (carbon), blue (nitrogen), red (oxygen), and orange (chlorine). Manganese ions (Mn1 and Mn2) are shown as green spheres. The carbon atoms of key active site residues are colored magenta, and the carbon atoms of other residues interacting with the compound or discussed in the text are colored cyan. An ordered water molecule (H$_2$O^{122}) is shown as a red sphere. Black dotted lines represent molecular interactions less than 3.2 Å away. In the case of compounds **2** and **5**, two molecules (yellow labels A and B) are bound in the PA$_N^{\Delta Loop}$ active site. Gray arrows (panels **B** and **C**) show the movement of helix-α3 residue Tyr24 compared with the structure of PA$_N^{\Delta Loop}$-Apo. The atomic coordinates and structure factors for PA$_N^{\Delta Loop}$ bound to compounds **1**–**6** have been deposited in the Protein Data Bank as PDB entries 4E5F, 4E5G, 4E5H, 4E5I, 4E5J, and 4E5L, respectively.
doi:10.1371/journal.ppat.1002830.g004

Kowalinski and coworkers also describe the structure of PA$_N$ bound to compound **2** and reveal an identical mode of binding [31]. However, they did not observe the second bound molecule, and we suggest that this is due to the higher concentration of **2** used in our structural studies. To confirm the stoichiometry of binding of compound **2** at the higher concentration, we carried out ITC experiments (Fig. S4). Analysis of the data strongly supports a 1:2 molar ratio for PA$_N$:compound **2** (N = 1.86, Fig. S4A), and an alternative analysis using a sequential binding model (Fig. S4B) also supports the second bound molecule of **2**, albeit with a nearly 100-fold lower affinity. These ITC analyses are therefore consistent with the structures in both studies where one or two molecules bind PA$_N$ depending on the concentration of compound **2**.

Compound **3** binds in a similar orientation as **2**, with the carboxylic acid interacting with Lys134 (Fig. 4C). The increased potency of **3** is likely due to the additional interactions formed by the benzylpiperidine and chlorobenzyl groups that splay in opposite directions perpendicular to the dioxobutanoic acid. The chlorobenzyl group engages the pocket occupied by the phenyl groups of molecules A and B in **2** (Fig. 4). The piperidine moiety directs the benzyl group into a narrow pocket comprising Arg84, Trp88, Phe105, and Leu106 (Fig. 4C). Although the electron density for **3** was relatively poor (Fig. S2), our model is supported by several lines of evidence. First, molecular docking of **3** into the PA$_N$ active site yields a strikingly similar orientation to that found in our crystallographic model (Fig. S5). Second, the chlorobenzyl group causes a similar movement in Tyr24 that is seen for **2**, which suggests that **3** also binds via an induced-fit mechanism

(Figs. 4, S3). Finally, mutation of Thr20 to alanine within the pocket occupied by the chlorobenzyl group caused a 3-fold reduction in virus inhibition in cell culture and a 2–3-fold reduction in inhibition of transcription by **3** (L-742,001) [18]. In our PA$_N^{\Delta Loop}$ construct, residue 20 is naturally an alanine, and a reduced affinity for **3** could explain the weak electron density for the chlorobenzyl group. We hypothesize that the larger threonine side chain mediates tighter interactions with the chlorobenzyl group and thereby increases affinity and inhibition.

Kowalinski and coworkers report the structure of PA$_N$ bound to compounds related to **3** [31], but the most closely-related compound (R05-2) adopts a significantly different orientation. The cyclohexane group of R05-2 is rotated 180° to coincide with the chlorobenzyl group of **3**, and the chlorobenzyl group of R05-2 enters a completely different pocket. The orientation of R05-2 is incompatible with the electron density of **3** and the reverse is also true [31]. The difference in conformations is not entirely surprising because Kowalinski and coworkers demonstrate that a similar compound (R05-3) binds in two distinct conformations [31]. We suggest that these compounds may adopt various conformations within the large PA$_N$ active site cleft depending on the microenvironment.

Prediction and Characterization of Three Additional PA$_N$ Endonuclease Inhibitors

Two-metal active sites similar to the one observed in PA$_N$ are present in many enzymes that process nucleic acids, and they

mediate a common catalytic reaction [33]. Raltegravir is an antiretroviral drug developed to treat HIV infections, and it targets the two-metal active site of HIV integrase [34]. The drug is built around a central pyrimidinol ring scaffold that contains in its plane three adjacent oxygen atoms similar to compounds **1**–**3**, and these oxygen atoms also coordinate the two-metal center in the active site of foamy virus integrase [35,36]. In keeping with our hypothesis that the pyrimidinol scaffold can serve as a general inhibitor of two-metal enzymes [37], we predicted that compounds **4** and **5**, which also contain the pyrimidinol scaffold (Fig. 2), would inhibit PA_N activity, and showed this to be the case (Fig. 3). Structural characterization of the two compounds bound to PA_N (Table 1) confirmed their interaction with the two Mn^{2+} ions, but we were surprised to find that their carboxyl groups are not in same location as the carboxyl group in compounds **2** and **3** (Figs. 4, S2). Compared with **2** and **3**, the pyrimidinol scaffold is flipped by $180°$ and there is no electrostatic interaction between the carboxyl groups and Lys134. We suggest that the flipped orientation of compounds **4** and **5** is necessary to maintain the optimal metal coordination for Mn1 (see discussion).

The imidazole and phenyl moieties of compounds **4** and **5**, respectively, show no obvious interactions with the PA_N active site cleft, but similar to what we observed with compound **2**, a second molecule (B) of compound **5** π-stacks onto molecule A (Figs. 4E, S2E). Molecule B is rotated $180°$ compared to molecule A and they interact via π-stacking interactions between the pyrimidinol and phenyl groups. Molecule B is further stabilized by hydrogen-bonding and ionic interactions with Lys34 and Arg124 (Fig. 4E). Attempts to determine the binding stoichiometry of compound **5** using ITC were not successful due to compound solubility problems, but similar to compound **2**, the electron density is unequivocal.

Finally, two recent studies have identified several compounds, including marchatins, green tea catechins, and dihydroxy phenethylphenylphthalimides, that inhibit PA_N endonuclease activity and influenza virus growth [27,28,38,39]. The common moiety in these inhibitors is a dihydroxyphenethyl group, and we predicted that dihydroxybenzoic acid (compound **6**), which contains this moiety and has oxygen atoms in positions similar to those in compounds **4** and **5**, would be able to bind and inhibit PA_N (Fig. 2). Although the compound shows little ability to inhibit PA_N endonuclease activity (Fig. 3F), we were able to determine the structure of **6** bound to PA_N at a resolution of 2.50 Å (Table 1). Compound **6** interacts with the two Mn^{2+} ions in the same orientation as the pyrimidinol scaffold (Figs. 4F, S2F). These data suggest that the dihydroxyphenethyl group binds to the PA_N active site in the same manner as **4** and **5**, but that additional interactions available in the marchatins, green tea catechins, and dihydroxy phenethylphenylphthalimides are required to inhibit PA_N activity. Indeed, Kowalinski and coworkers report the structure of PA_N bound to the green tea catechin EGCG and this reveals these additional interactions [31].

Structural Basis of the SAR of Known Inhibitors

Figure 5 shows the inhibitory concentration (IC_{50}) values of a series of compounds related to **1**, including the natural product inhibitor Flutimide (**7**) [29,30]. Using the co-crystal structure with **1** (Fig. 4), we analyzed the SAR of this series. We suggest that the increased potency of Flutimide compared with **1** is the result of an interaction between one of the two isobutyl groups and Tyr24, and that this is further enhanced by the larger fluorobenzyl group of **8**, as reflected by the 6-fold increase in potency compared with Flutimide. Docking studies support our hypothesis that compounds **7** and **8** form molecular interactions with Tyr24 (Fig. S5).
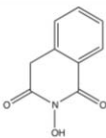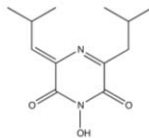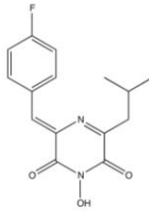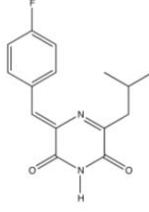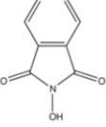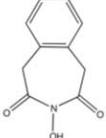
Compound	Structure	Reported IC_{50} (μM)
1		15.0^a
7 (Flutimide)		5.5^b
8		0.9^b
9		$>365^b$
10		$>500^a$
11		$>1000^a$

Figure 5. Reported IC_{50} values of Flutimide, Flutimide-related, and *N*-hydroxyimide inhibitors determined in an *in vitro* transcription assay with influenza A polymerase. ^{a}Published results in an influenza virus *in vitro* transcription assay [29]. ^{b}Published results in an influenza virus *in vitro* transcription assay [30]. doi:10.1371/journal.ppat.1002830.g005

Finally, the presence and positioning of all three Mn^{2+}-binding oxygen atoms is confirmed by the lack of potency observed in compounds **9**–**11**.

Our co-crystal structures with **2** and **3** also provide molecular insights into the SAR of several 4-substituted 2,4-dioxobutanoic acids (Fig. 6) [15,26]. The addition of an extra phenyl group to **2** as seen in **12** results in a 6-fold gain in potency, and this can be rationalized by additional interactions with Tyr24. Consistent with this, replacement of the phenyl group in **2** with shorter hydrophobic groups in **13** and **14** results in 2.6- and 14-fold reductions in potency, respectively. The importance of the electrostatic interaction between the carboxyl group and Lys134 is confirmed by **15**, in which the replacement of the carboxyl with a methyl ester severely compromises potency. Similar to the effect seen in the Flutimide-related compounds, deletion or repositioning
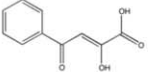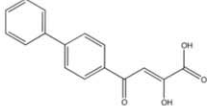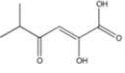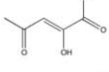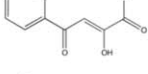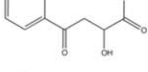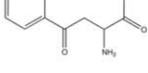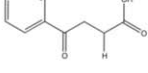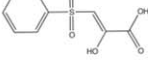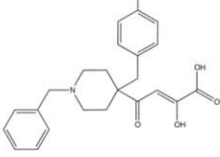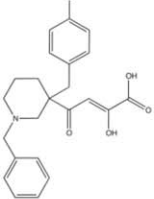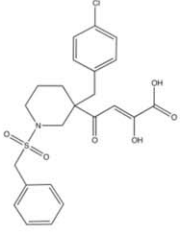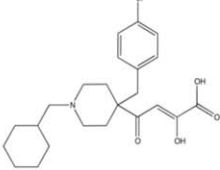
Compound	Structure	Reported IC$_{50}$ (μM)
2 (DPBA)		21.3[a]
12		3.7[a]
13		56.7[a]
14		307.0[a]
15		>500[a]
16		>500[a]
17		>500[a]
18		>500[a]
19		>500[a]
3 (L-742,001)		0.43[b]
20 (L-735,882)		1.10[a,b]
21		0.19[a]
22		0.32[b]

Figure 6. Reported IC$_{50}$ values of 4-substituted 2,4-dioxobutanoic acid inhibitors determined in an *in vitro* transcription assay with influenza A polymerase. [a]Published results in an influenza virus *in vitro* transcription assay [15]. [b]Published results in an influenza virus *in vitro* transcription assay [26].
doi:10.1371/journal.ppat.1002830.g006

of metal-coordinating oxygen atoms eliminates activity (**16–19**). Compounds **20**, **21** and **22** were found to inhibit *in vitro* transcription and endonuclease activity with high potency similar to **3** (Fig. 6), and to exhibit dose-dependent inhibition of viral replication in cell culture [15,26]. While the additional groups at the 4-position of the dioxobutanoic acid scaffold clearly increase the activity of these compounds, the differences between our structure with compound **3** and the structures in the accompanying article with **20**, **21** and **22** [31] make it difficult to characterize their SAR. However, the observed conformational differences do suggest that the potencies of these compounds can be significantly improved now that structural information is available.

Finally, we recently used a fluorescence polarization assay to identify several additional PA$_N$ inhibitors that are related to **4** and **5** (Fig. 7) [40]. In compounds **23**, **25** and **26**, the carboxylic acid has been replaced with marginal impact on potency as reflected in the K_i values. This is consistent with the co-crystal structures of **4** and **5**, in which the carboxylic acid does not interact with Lys134 and there is available space for the substituent (Fig. 4). The significant gain in potency of **26** may reflect an interaction with Tyr24 as observed in **2** and **3** (Fig. 4). The increase in potency of **26** is also reflected in the increase in antiviral activity of this compound (Figs. 7, S6).

Discussion

Our studies, and those described by Kowalinski and coworkers in the accompanying article [31], provide the first molecular insights into the mechanism of inhibition of the essential influenza enzyme PA endonuclease, and we have confirmed that it represents an ideal target for drug discovery. Previous mutagenesis studies have shown a direct correlation between PA$_N$ endonuclease activities and RdRp transcription activities, suggesting that the isolated PA$_N$ domain contains the same structure in the context of the intact RdRp [12,17,19]. Our biochemical studies show that inhibitors of RdRp transcription also inhibit PA$_N$ endonuclease activity, and this validates the use of the isolated PA$_N$ endonuclease domain for drug development.

Our structural studies provide the framework to develop novel inhibitors of the influenza virus PA endonuclease. However, two-metal active sites are ubiquitous in enzymes that process nucleic acids, and it may be challenging to develop drugs that specifically target PA$_N$ endonuclease. We therefore analyzed the PA$_N$ active site for conserved and unique features for drug discovery by aligning ~13,000 PA amino acid sequences to identify the consensus sequence for PA$_N$ of influenza types A, B, and C (Fig. 8A). Thirty residues are highly conserved and 17 are more than 99.9% identical. Unsurprisingly, most are in the active site pocket and include the metal-binding residues His41, Glu80, Asp108, and Glu119 and the catalytic residue Lys134 (Fig. 8B). The central scaffolds of our characterized inhibitors interact with these residues and are likely to be resistant to mutation but are unlikely to be useful for specificity.

Our studies have shown that interactions with residues further away from the two-metal center substantially increase potency. The same conclusion has been drawn by Kowalinski and coworkers who specifically identified four pockets that can be exploited for inhibitor optimization [31]. Figure 8C maps out how
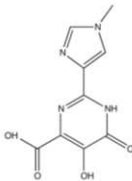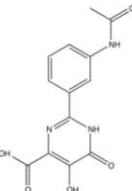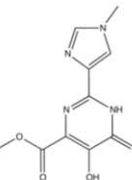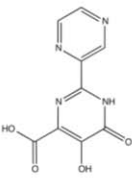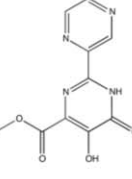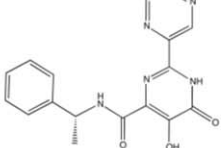
Compound	Structure	Reported FP K_i (μM)[a]	Antiviral Activity IC$_{50}$ (μM)[b,c]	Cytotoxicity CC$_{50}$ (μM)[d,e]
4		5.01	>50[b]	>60[d]
5		18.7	>50[b]	48.7±1.2[d]
23		20.3	>50[b]	53.2±0.9[d]
24		1.1	>50[c]	>60[e]
25		8.00	>50[b]	>60[d]
26		0.29	12.68±0.08[c]	>60[e]

Figure 7. Reported PA$_N$ binding activities, antiviral activities, and cytotoxicities of compounds 4 and 5 and related compounds.
[a]Published results in a competitive binding fluorescence polarization assay with PA$_N$ [40]. [b,c]Antiviral activity as measured by inhibition of viral plaque formation in this study[b] or previously[c] [40]. [d,e]Compound cytotoxicity in MDCK cells after 72 hours as measured in this study[d] or previously[e] [40].
doi:10.1371/journal.ppat.1002830.g007

compounds **1**–**6** engage these pockets, and it can be seen that none of the compounds bind pockets 1 and 2, which only appear to become available upon side-chain rotation and inhibitor binding [31]. However, our structures reveal two additional pockets 5 and 6. Compounds **2** and **3** occupy pocket 3 and interact with Tyr24, which is a highly conserved aromatic residue. The biological role of Tyr24 is revealed in the studies of Kowalinski and coworkers which show that it forms a crucial stacking interaction with the base of the mononucleotide [31]. The new pocket 5 is revealed by the binding of the benzylpiperidine group of compound **3**; it comprises conserved residues Arg84, Trp88, Phe105, and Leu106, and is an excellent target for further exploration (Figs. 4C, 8C). The same is true for the new pocket 6 that engages the acetamide

group of compound **5** and comprises highly conserved residues Thr123, Tyr130, Lys134 and Lys137 (Figs. 4E, 8C). Mutation of Arg84, Tyr130, or Lys137 to Ala reduces but does not eliminate endonuclease activity, suggesting that inhibitor resistance could develop, although possibly at a cost to virus fitness [12,19]. Similarly, the interactions between molecule B of compound **5** and pocket 4 residues Lys34 and Arg124 are unlikely to be useful for drug development because these residues are not well conserved. However, π-stacking interactions have been shown to be very productive in terms of increasing potency [35,41,42], and Tyr24, His41, F105, Tyr130, and F150 offer potential opportunities. These data reveal the potential for the use of growing and linking strategies to design potent inhibitors.
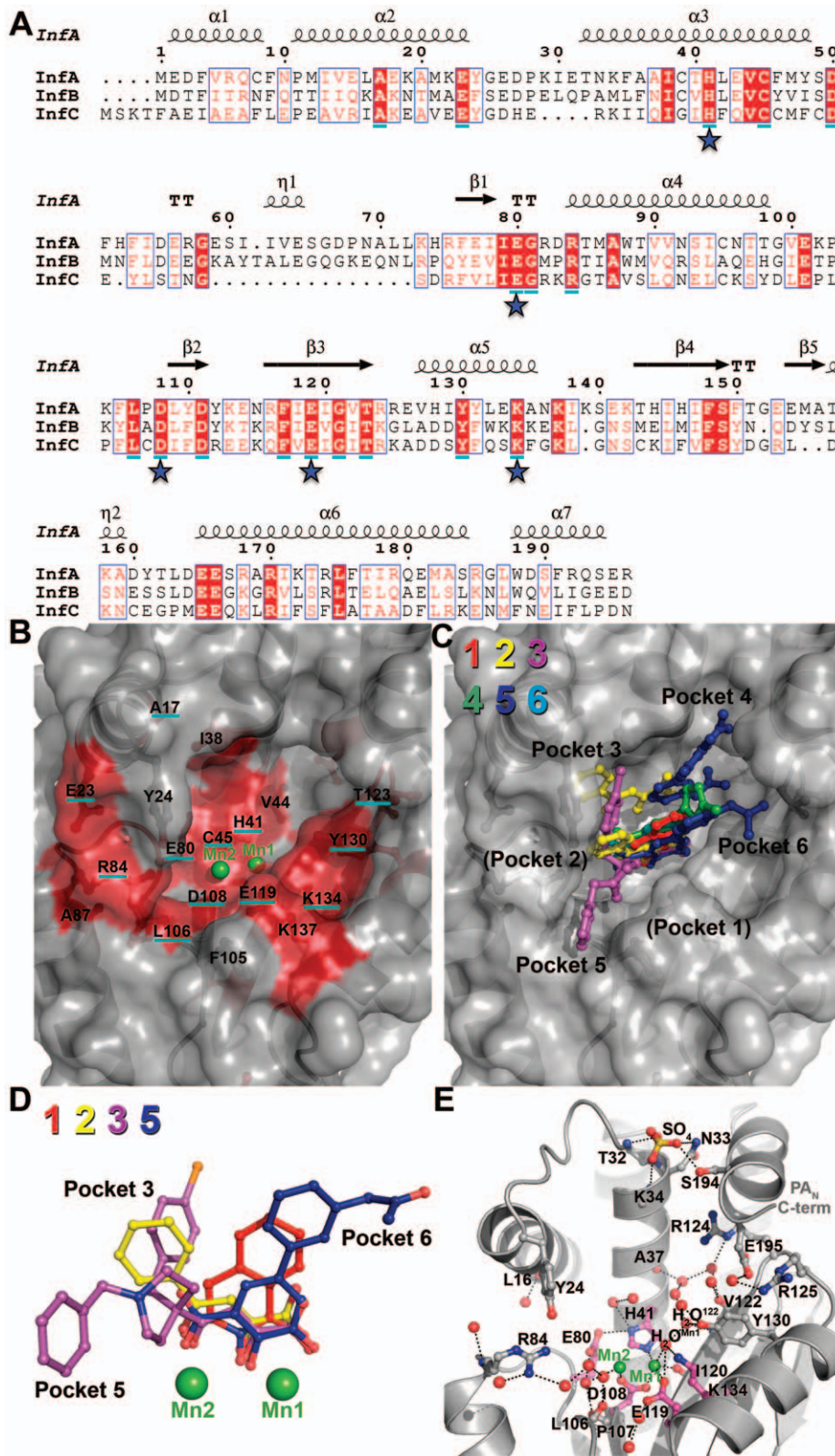
Figure 8. Conserved residues and ordered water molecules in the PA$_N$ active site cleft. (A) Sequence alignment of PA$_N$ from influenza A, B, and C. Consensus sequences were determined from more than 13,000 sequences using the online database www.fludb.org. The secondary structure of PA$_N$ from influenza A is shown above the sequence alignment. Residues in a solid red background are identical between the influenza A, B, and C consensus sequences. Residues that are >99.9% conserved in all sequences analyzed are underlined in cyan. Stars indicate key active site residues. (**B**) Surface representation of the PA$_N$$^{\Delta Loop}$ active site cleft. Manganese ions (Mn1 and Mn2) are shown as green spheres. The highly conserved cleft is colored red. Residues that are identical between influenza A, B, and C consensus sequences are not underlined, and residues that are >99.9% conserved are underlined in cyan. (**C**) Surface representation of PA$_N$$^{\Delta Loop}$ active site cleft with overlays of compounds **1** (red), **2** (yellow), **3** (purple), **4**

(green), **5** (blue), and **6** (cyan). The compounds occupy four (3–6) of the six binding pockets discussed in the text. The orientation and depicted surface are identical to those shown in panel **B**. (**D**) Superposition of bound compounds **1, 2, 3 and 5** (same coloring as panel **C**) after structural alignment of the entire PA$_N^{\Delta Loop}$ domain. For clarity, molecules B of **2** and **5** are not shown. Also not shown for clarity are compounds **4** and **6** because their metal-binding scaffolds overlay perfectly with **5**. Manganese ions (Mn1 and Mn2) are shown as green spheres. (**E**) Ordered water molecules found in at least three of the four molecules in the crystallographic asymmetric unit are shown as red spheres. PA$_N^{\Delta Loop}$ is shown as gray cartoon. Manganese ions (Mn1 and Mn2) are shown as green spheres. Key active site residues are shown in magenta carbon atoms and other residues interacting with the compound or discussed in the text are shown in gray carbon atoms. A sulfate ion is shown as ball-and-stick and colored yellow (sulfur) and red (oxygen). This sulfate is bound at the same location as a predicted phosphate group of nucleic acid in a model of the PA$_N$-substrate complex [25]. Black dotted lines represent molecular interactions less than 3.2 Å away.
doi:10.1371/journal.ppat.1002830.g008

The entropic contribution to binding can be substantial when ordered water molecules are displaced [43,44,45], and the PA$_N$ active site offers opportunities in this regard. PA$_N$ contains a large, deep active site (over 3000 Å^3) with several ordered water molecules, 17 of which are found in at least three of the four PA$_N$ molecules in the asymmetric unit (Fig. 8E). A large network of water molecules near Val122 becomes displaced by molecule B of compound **5**, and a network of four water molecules between Mn2 and Arg84 is displaced by the benzylpiperidine group of compound **3**, and both can be targeted for inhibitor optimization. Ordered water molecules can also be mimicked by oxygen atoms introduced during inhibitor optimization (see for example [46]). Our studies provide an example of this. One water molecule (H$_2$O^{Mn1}) that interacts with Mn1, Glu119, and Lys134 becomes displaced by an oxygen atom from compounds **1**–**6** (Figs. 8D, 8E). H$_2$O^{Mn1} also forms a hydrogen bond with water molecule H$_2$O^{122}, which in turn forms hydrogen bonds with Val122 (backbone amide), Tyr130, and another water molecule. Modification of inhibitors that displace H$_2$O^{122} but preserve its hydrogen bonds should significantly improve inhibitor binding via gains in both entropy and enthalpy.

Another important consideration in the design of optimal inhibitors is the location and coordination sphere of each Mn^{2+} ion in the PA$_N$ active site. Detailed structural analyses on the *Bacillus halodurans* RNase H revealed that the distance between the metal ions changes at different stages of phosphodiester hydrolysis [47,48]. Consistent with this is the observation that the metals are approximately 2.9 Å apart in PA$_N^{\Delta Loop}$–Apo and move to 3.8–4.0 Å apart when an inhibitor is bound. This mobility seems to occur in Mn2 because Mn1 is in a similar location in both the unbound and inhibitor-bound structures. Our data suggest that the inhibitor-bound form of PA$_N$ represents the enzyme-substrate complex stage in which the metals are separated by about 4.0 Å [47,48]. Thus, computational modeling or docking of inhibitors may best be suited with the inhibitor-bound form of PA$_N$ and Mn^{2+} ions.

Furthermore, metal coordination appears to play an important role in compound binding. Specifically, the compound oxygen atoms that coordinate Mn1 in all the complexes described here and in the accompanying article [31] are separated by two atoms (Fig. 8D), and this allows them to ideally contribute to the octahedral geometry completed by the Mn1-coordinating oxygen atoms from H41, D108, E119, and I120.

Finally, our studies support the potential for developing antiviral inhibitors that target the endonuclease activity of other negative strand and cap-snatching segmented RNA viruses, specifically the *Orthomyxoviridae*, *Bunyaviridae*, and *Arenaviridae* families. Recent crystal structures of the endonuclease domains from La Crosse orthobunyavirus L protein and lymphocytic choriomeningitis virus L protein reveal clear structural homology to the influenza A virus PA$_N$ endonuclease domain with dependence on manganese ions for activity [32,49] (Fig. S7). However, low sequence homology and structural variation between virus family endonucleases suggest opportunities for developing virus family-specific inhibitors.

Methods

Chemical Synthesis of Inhibitors

The activity, but not synthesis, of compound **1** (an *N*-hydroxyimide) was described previously [29]. We produced compound **1** using synthetic conditions described by Birch et al. [50]. Briefly, hydroxylamine HCl (0.9 M) was added to anhydride (1.0 M) in pyridine in a microwavable vessel. The reaction was incubated under a nitrogen atmosphere at 120°C for 60 min under high absorption in a Biotage initiator 60 microwave. Methyl *tert*-butyl ether was used to precipitate the hydroxylsuccinate product that was isolated via filtration. Compound **1** was further re-crystallized with methanol:chloroform. Compounds **2** (2,4-dioxo-4-phenylbutanoic acid, or DPBA) and **3** (L-742,001) were prepared with a slight modification to published methods [15]. Instead of producing a methyl ester intermediate, a *tert*-butyl ester intermediate was produced and then converted to the acid form with trifluoroacetic acid. Compound **4** (5-hydroxy-2-(1-methyl-1H-imidazol-4-yl)-6-oxo-1,6-dihydropyrimidine-4-carboxylic acid) and compound **5** (2-(3-acetamidophenyl)-5-hydroxy-6-oxo-1,6-dihydropyrimidine-4-carboxylic acid) were synthesized in a similar manner as related compounds described previously [37,51]. Compound **6** (dihydroxybenzoic acid) was purchased from Sigma-Aldrich and used without further purification.

Compound purities were determined by ultra-high-pressure liquid chromatography on a BEH C18 column with a gradient elution of solvent A (0.1% formic acid in water) to solvent B (0.1% formic acid in acetonitrile) using an evaporative light scattering detector (ELSD) and an ultraviolet (UV, 210 to 400 nm) detector. Purities are: compound **1** (ELSD: >99%, UV: 97%), compound **2** (ELSD: 92%, UV: 85%), compound **3** (ELSD: >99%, UV: 98%), compound **4** (ELSD: >99%, UV: 81%), compound **5** (ELSD: >99%, UV: 97%), and compound **6** (ELSD: >99%, UV: 92%). Nuclear magnetic resonance (NMR) spectra measured on a Brooker-400 (400 MHz) spectrometer showed that all compounds are consistent with their assigned structures. NMR experimental results have previously been published [40].

The tautomeric form of compound **2** shown in Figure 2 was confirmed by solving the high resolution (0.84 Å) x-ray crystal structure of the compound alone.

Cloning

PA$_N$ (residues 1–209) or PA$_N^{\Delta Loop}$ (residues 1–50 and 73–196 with a 3-residue linker Gly-Gly-Ser between residues 50 and 73) from H5N1 influenza virus A/Vietnam/1203/2004 (Accession #AY818132) was cloned between the NcoI and NotI sites in the pET52b plasmid in-frame with a C-terminal thrombin cleavage site followed by a 10-histidine purification tag.

PA$_N$ and PA$_N^{\Delta Loop}$ Protein Production

PA$_N$ and PA$_N^{\Delta Loop}$ were expressed and purified with modifications to previously published methods [16]. The recombinant proteins were overexpressed in *E. coli* strain BL21 (DE3), and the proteins were purified from soluble lysates by HisTrap affinity

chromatography. The 10-histidine purification tags were removed by digestion with biotinylated thrombin, which was later removed by incubation with streptavidin-agarose beads. Undigested protein was removed with cobalt-NTA beads. PA_N and $PA_N^{\Delta Loop}$ were then purified by size-exclusion chromatography on a Superdex 75 column in 10 mM Tris pH 8.0, 100 mM NaCl, and 1 mM DTT. Proteins were concentrated to 5–10 mg/ml.

In Vitro Endonuclease Activity Assay

In vitro endonuclease activity assays were done with modifications to previously published methods [16]. Single-stranded DNA plasmid M13mp18 (50 ng/µl) was incubated in digestion buffer (10 mM Tris pH 8.0, 100 mM NaCl, 10 mM β-mercaptoethanol, and 2.5 mM $MnCl_2$) in the presence of 3, 10, or 30 µM PA_N or $PA_N^{\Delta Loop}$ for 2 h at 37°C. The reaction was stopped by adding 50 mM EDTA. For studies with inhibitors, 10 mM inhibitor in DMSO was diluted 3-fold in series with DMSO and then used at a 10% concentration in enzymatic reactions containing 15 µM PA_N. Reaction products were resolved on a 1.0% agarose gel stained with ethidium bromide.

Crystal Structure Determination

$PA_N^{\Delta Loop}$ protein crystals were grown by the hanging-drop vapor diffusion method at 18°C in a well solution of 1.50 M ammonium sulfate, 2% PEG1500, 0.1 M Tris pH 8.0, and 1 mM $MnCl_2$. Crystals grew after 3–4 days. Crystals were transferred into a soak solution (1.65 M ammonium sulfate, 2% PEG1500, 0.1 M Tris pH 8.0, 5 mM $MnCl_2$, and 10 mM $MnCl_2$) containing ~20 mM inhibitor and incubated overnight at 18°C. Crystals were quickly transferred into a cryo-protection solution (0.4 M ammonium sulfate, 2% PEG1500, 0.1 M Tris pH 8.0, 5 mM $MnCl_2$, 10 mM $MnCl_2$, and 25% PEG400) containing 10 mM inhibitor before flash freezing in liquid nitrogen. In the case of $PA_N^{\Delta Loop}$-Apo, crystals were mock-soaked in soak solution without inhibitor and cryo-protected without inhibitor.

Diffraction data were collected at cryogenic temperature at X-ray wavelength 1.00 Å from the Southeastern Regional Collaborative Access Team's 22-ID and 22-BM beamlines at the Advanced Photon Source (Argonne National Laboratory, Chicago, IL). Data processing and reduction were completed with HKL-2000 software [52].

The $PA_N^{\Delta Loop}$-Apo structure was determined by molecular replacement using the program Phaser [53]. A solution was obtained by using a model of the avian PA_N crystal structure (PDB code 3EBJ, residues 1–50 and 73–196) [17]. The model was corrected to encode PA residues from A/Vietnam/1203/2004, and residues 80, 108, and 119 were mutated to alanine to remove model bias from these metal-coordinating active-site residues. Simulated annealing was then done using Phenix [54]. Residues 80, 108, and 199 were corrected and model building was performed using Coot [55] followed by restrained refinement using the CCP4 software suite's REFMAC5 [56]. Refinement was monitored by following the R_{free} value calculated for a random subset (5%) of reflections omitted from refinement. For the $PA_N^{\Delta Loop}$-inhibitor structures, simulated annealing was done with $PA_N^{\Delta Loop}$-Apo without Mn^{+2} ions and with residues 80, 108, and 119 mutated to alanine to remove model bias.

Isothermal Titration Calorimetry Assays

Purified PA_N protein was dialyzed against 25 mM HEPES pH 8.0, 100 mM NaCl, and 1 mM $MnCl_2$. ITC titrations were performed with an Auto-iTC200 Isothermal Titration Calorimeter (MicroCal) at 25°C. Nineteen injections of 2 µl each of 2 mM compound **2** were titrated into 100 µM protein solution. 5% DMSO was added to the ITC buffer for the titration experiment. Data were analyzed using MicroCal Origin 7.0 software using a One-Site binding model and Sequential Binding Sites model with two sites. The experiments were performed independently twice and showed very similar results.

Docking of Compounds

Docking of compounds **3**, **7** (Flutimide), and **8** into $PA_N^{\Delta Loop}$ active site was performed by Glide module in Schrodinger software. For compound **3**, the docking model was generated from the crystal structure of the $PA_N^{\Delta Loop}$–compound **2** complex, with the 2,4-dioxobutanoic acid group defined as the reference core structure for guiding the corresponding functional group in compound **3** into the correct orientation (tolerance set to 0.8 Å RMSD). For compounds **7** and **8**, the docking model was generated from the crystal structure of the $PA_N^{\Delta Loop}$–compound **1** complex, with the *N*-hydroxyimide group defined as the reference core structure for guiding the corresponding functional group in compounds **7** and **8** into the correct orientation (tolerance set to 0.8 Å RMSD). Two Mn^{2+} ions in the active site were kept as part of the protein. The binding pocket is defined as residues within 20 Å radius of the reference core structure. All water molecules were deleted from the protein structure before docking. The compound geometries were built and optimized by SYBYL program. The standard precision of Glidescore scoring functions was used to rank binding poses.

Antiviral Activity Assays

Antiviral activity assays were carried out exactly as done previously [40]. Briefly, avian H1N1 influenza A virus (A/PuertoRico/8/34) grown in embryonated eggs was used for infection [50–100 PFU of PR8 virus per well (MOI = 0.0001)] in Madin-Darby canine kidney (MDCK) cells (3×10^5 cells/well). After 1 h, each well was overlaid with medium containing agarose and compound (at least 10 concentrations of each compound). After 72 h, plaques were visualized with crystal violet and counted. The concentration of compound required for 50% inhibition of plaque formation (IC_{50}) was determined for triplicate measurements by nonlinear least-squares analysis using GraphPad Prism 4.03.

Compound Cytotoxicity Assays

Compound cytotoxicity assays were carried out exactly as done previously [40]. Briefly MDCK cells (3×10^5 cells/mL, 20 µL per well) were incubated with compound at 2-fold serial dilutions from 60 µM. The negative control was 0.6% DMSO and the positive control was 60 µM staurosporine. After 72 h, 20 µL CellTiter-Glo reagent was added and luminescence was measured. The concentration of compound required to decrease cell viability by 50% (CC_{50}), was determined for triplicate measurements by nonlinear least-squares analysis using GraphPad Prism 4.03.

Accession Numbers

The atomic coordinates and structure factors have been deposited in the Protein Data Bank, www.pdb.org, under accession numbers 4E5E, 4E5F, 4E5G, 4E5H, 4E5I, 4E5J, and 4E5L.

Supporting Information

Figure S1 $PA_N^{\Delta Loop}$ crystal packing and active site manganese ions. (**A**) Four $PA_N^{\Delta Loop}$ molecules in the crystallographic asymmetric unit. The Gly-Gly-Ser linker that replaces a 22 amino acid loop is shown as magenta spheres. Manganese ions in the active sites are shown as green spheres. (**B**) Simulated-annealing

Fo-Fc omit map (brown) contoured at 3.0 σ around the manganese ions in the PA$_N^{\Delta Loop}$ active site from crystals soaked in the absence of magnesium ions.
(TIF)

Figure S2 Electron densities of compounds **1**–**6** (**A**–**F**, respectively). Each panel shows the final 2Fo-Fc electron density map (blue) and the simulated-annealing Fo-Fc omit map (brown) contoured at 1.0 σ and 3.0 σ, respectively. PA$_N^{\Delta Loop}$ is shown as cartoon and colored gray. Compounds are shown as ball-and-stick models and are colored yellow (carbon), blue (nitrogen), red (oxygen), and orange (chlorine). Manganese ions (Mn1 and Mn2) are shown as green spheres.
(TIF)

Figure S3 Induced-fit binding by compounds **2** and **3**. (**A**) Comparison of PA$_N^{\Delta Loop}$-Apo (gray) and PA$_N^{\Delta Loop}$-compound **2** (purple) structures reveals the movement of Tyr24 on helix-α3. Two molecules of compound **2** (yellow labels A and B) are shown as ball-and-stick models and are colored yellow (carbon), blue (nitrogen), and red (oxygen). Manganese ions (Mn1 and Mn2) are shown as green spheres. The gray arrow shows the movement of helix-α3 residue Tyr24. (**B**) Comparison of PA$_N^{\Delta Loop}$-Apo (gray) and PA$_N^{\Delta Loop}$-compound **3** (purple) structures, displayed as in panel **A**. (**C**) PA$_N^{\Delta Loop}$-Apo active site colored by B-factor from blue (B-factor ~20) to white to red (B-factor ~50).
(TIF)

Figure S4 Isothermal titration calorimetry (ITC) binding of PA$_N$ and compound **2**. (**A**) One-site model. (**B**) Sequential binding site model with two sites. In the lower panels, the solid squares represent experimental data, and the continuous lines correspond to the model fits. Note that binding by compound **2** is endothermic and is entropically favorable, possibly by displacement of water molecules shown in Figure 8E.
(TIF)

Figure S5 Docking models of **3**, **7** (Flutimide), and **8** in the PA$_N$ active site. (**A**–**B**) Comparison of the crystal structure with compound **3** (**A**) and the docked model with compound **3** (**B**). (**C**–**F**) Comparison of the crystal structure with compound **1** (**C**) and the docked model with compound **7** (Flutimide) (**D**) and compound **8** (**E**–**F**). Panels (**E**) and (**F**) represent two docked orientations of compound **8**. In all panels, PA$_N^{\Delta Loop}$ is shown as

cartoon and colored gray. Manganese ions (Mn1 and Mn2) are shown as green spheres. Tyr24 that is predicted to interact with compounds **7** and **8** is shown as cyan. Compounds are shown as ball-and-stick models and are colored blue (nitrogen), red (oxygen), light orange (chlorine), and violet (fluorine), with yellow and orange carbons, respectively, in the crystal structures and the docked structures. Docking scores for compounds **3**, **7** and **8** are −9.3 kcal/mol, −4.5 kcal/mol, and −5.2 kcal/mol, respectively. Docking scores for compound **8** are the same for the two orientations observed in panels (**E**) and (**F**).
(TIF)

Figure S6 Antiviral activities of compounds listed in Figure 7. Antiviral activity was measured by inhibition of viral plaque formation in MDCK cells after 72 hours. IC$_{50}$ values are reported in Figure 7.
(TIF)

Figure S7 Endonuclease domains from other cap-snatching RNA viruses. Endonuclease domain structures from the influenza A virus PA protein (Orthomyxovirus), La Crosse orthobunyavirus L protein (Bunyavirus), and lymphocytic choriomeningitis virus L protein (Arenavirus). Structures are shown as cartoon and colored blue-to-red rainbow from N- to C-termini. Key active site residues are colored magenta and are shown as ball-and-stick. The coordinates for the bunyavirus and arenavirus structures are from PDB entries 2XI5 and 3JSB, respectively.
(TIF)

Acknowledgments

Author Contributions

Conceived and designed the experiments: RMD PJS SWW. Performed the experiments: RMD PJS BMB MY. Analyzed the data: RMD PJS JB RJW TRW SWW. Contributed reagents/materials/analysis tools: JB. Wrote the paper: RMD SWW.

References

1. Reid AH, Taubenberger JK, Fanning TG (2001) The 1918 Spanish influenza: integrating history and biology. Microbes Infect 3: 81–87.
2. Garten RJ, Davis CT, Russell CA, Shu B, Lindstrom S, et al. (2009) Antigenic and genetic characteristics of swine-origin 2009 A(H1N1) influenza viruses circulating in humans. Science 325: 197–201.
3. WHO (2012) Avian influenza in humans. Available: http://www.who.int/csr/disease/avian_influenza/.
4. Imai M, Watanabe T, Hatta M, Das SC, Ozawa M, et al. (2012) Experimental adaptation of an influenza H5 HA confers respiratory droplet transmission to a reassortant H5 HA/H1N1 virus in ferrets. Nature 486: 420–8.
5. Herfst S, Schrauwen EJA, Linster M, Chutinimitkul S, de Wit E, et al. (2012) Airborne Transmission of Influenza A/H5N1 Virus Between Ferrets. Science 336: 1534–1541.
6. Stiver G (2003) The treatment of influenza with antiviral drugs. CMAJ 168: 49–56.
7. WHO (2012) Global Influenza Programme. Available: http://www.who.int/influenza/en/.
8. Hagen M, Chung TD, Butcher JA, Krystal M (1994) Recombinant influenza virus polymerase: requirement of both 5′ and 3′ viral ends for endonuclease activity. J Virol 68: 1509–1515.
9. Tiley LS, Hagen M, Matthews JT, Krystal M (1994) Sequence-specific binding of the influenza virus RNA polymerase to sequences located at the 5′ ends of the viral RNAs. J Virol 68: 5108–5116.
10. Guilligay D, Tarendeau F, Resa-Infante P, Coloma R, Crepin T, et al. (2008) The structural basis for cap binding by influenza virus polymerase subunit PB2. Nat Struct Mol Biol 15: 500–506.
11. Li ML, Rao P, Krug RM (2001) The active sites of the influenza cap-dependent endonuclease are on different polymerase subunits. Embo J 20: 2078–2086.
12. Hara K, Schmidt FI, Crow M, Brownlee GG (2006) Amino acid residues in the N-terminal region of the PA subunit of influenza A virus RNA polymerase play a critical role in protein stability, endonuclease activity, cap binding, and virion RNA promoter binding. J Virol 80: 7789–7798.
13. Biswas SK, Nayak DP (1994) Mutational analysis of the conserved motifs of influenza A virus polymerase basic protein 1. J Virol 68: 1819–1826.
14. Plotch SJ, Bouloy M, Ulmanen I, Krug RM (1981) A unique cap(m7GpppXm)-dependent influenza virion endonuclease cleaves capped RNAs to generate the primers that initiate viral RNA transcription. Cell 23: 847–858.
15. Tomassini J, Selnick H, Davies ME, Armstrong ME, Baldwin J, et al. (1994) Inhibition of cap (m7GpppXm)-dependent endonuclease of influenza virus by 4-substituted 2,4-dioxobutanoic acid compounds. Antimicrob Agents Chemother 38: 2827–2837.
16. Dias A, Bouvier D, Crepin T, McCarthy AA, Hart DJ, et al. (2009) The cap-snatching endonuclease of influenza virus polymerase resides in the PA subunit. Nature 458: 914–918.
17. Yuan P, Bartlam M, Lou Z, Chen S, Zhou J, et al. (2009) Crystal structure of an avian influenza polymerase PA(N) reveals an endonuclease active site. Nature 458: 909–913.
18. Nakazawa M, Kadowaki SE, Watanabe I, Kadowaki Y, Takei M, et al. (2008) PA subunit of RNA polymerase as a promising target for anti-influenza virus agents. Antiviral Res 78: 194–201.
19. Crepin T, Dias A, Palencia A, Swale C, Cusack S, et al. (2010) Mutational and metal binding analysis of the endonuclease domain of the influenza virus polymerase PA subunit. J Virol 84: 9096–9104.

20. Doan L, Handa B, Roberts NA, Klumpp K (1999) Metal ion catalysis of RNA cleavage by the influenza virus endonuclease. Biochemistry 38: 5612–5619.
21. He X, Zhou J, Bartlam M, Zhang R, Ma J, et al. (2008) Crystal structure of the polymerase PA(C)-PB1(N) complex from an avian influenza H5N1 virus. Nature 454: 1123–1126.
22. Obayashi E, Yoshida H, Kawai F, Shibayama N, Kawaguchi A, et al. (2008) The structural basis for an essential subunit interaction in influenza virus RNA polymerase. Nature 454: 1127–1131.
23. Sugiyama K, Obayashi E, Kawaguchi A, Suzuki Y, Tame JR, et al. (2009) Structural insight into the essential PB1-PB2 subunit contact of the influenza virus RNA polymerase. Embo J 28: 1803–1811.
24. Tarendeau F, Crepin T, Guilligay D, Ruigrok RW, Cusack S, et al. (2008) Host determinant residue lysine 627 lies on the surface of a discrete, folded domain of influenza virus polymerase PB2 subunit. PLoS Pathog 4: e1000136.
25. Zhao C, Lou Z, Guo Y, Ma M, Chen Y, et al. (2009) Nucleoside monophosphate complex structures of the endonuclease domain from the influenza virus polymerase PA subunit reveal the substrate binding site inside the catalytic center. J Virol 83: 9024–9030.
26. Hastings JC, Selnick H, Wolanski B, Tomassini JE (1996) Anti-influenza virus activities of 4-substituted 2,4-dioxobutanoic acid inhibitors. Antimicrob Agents Chemother 40: 1304–1307.
27. Iwai Y, Murakami K, Gomi Y, Hashimoto T, Asakawa Y, et al. (2011) Anti-influenza activity of marchantins, macrocyclic bisbibenzyls contained in liverworts. PLoS One 6: e19825.
28. Iwai Y, Takahashi H, Hatakeyama D, Motoshima K, Ishikawa M, et al. (2010) Anti-influenza activity of phenethylphenylphthalimide analogs derived from thalidomide. Bioorg Med Chem 18: 5379–5390.
29. Parkes KE, Ermert P, Fassler J, Ives J, Martin JA, et al. (2003) Use of a pharmacophore model to discover a new class of influenza endonuclease inhibitors. J Med Chem 46: 1153–1164.
30. Tomassini JE, Davies ME, Hastings JC, Lingham R, Mojena M, et al. (1996) A novel antiviral agent which inhibits the endonuclease of influenza viruses. Antimicrob Agents Chemother 40: 1189–1193.
31. Kowalinski E, Zubieta C, Wolkerstorfer A, Szolar OHJ, Ruigrok RWH, et al. (2012) Structural analysis of specific metal chelating inhibitor binding to the endonuclease domain of influenza pH1N1 (2009) polymerase. PLoS Pathog. In press.
32. Reguera J, Weber F, Cusack S (2010) Bunyaviridae RNA polymerases (L-protein) have an N-terminal, influenza-like endonuclease domain, essential for viral cap-dependent transcription. PLoS Pathog 6: e1001101.
33. Yang W, Lee JY, Nowotny M (2006) Making and breaking nucleic acids: two-Mg2+-ion catalysis and substrate specificity. Mol Cell 22: 5–13.
34. Summa V, Petrocchi A, Bonelli F, Crescenzi B, Donghi M, et al. (2008) Discovery of raltegravir, a potent, selective orally bioavailable HIV-integrase inhibitor for the treatment of HIV-AIDS infection. J Med Chem 51: 5843–5855.
35. Hare S, Gupta SS, Valkov E, Engelman A, Cherepanov P (2010) Retroviral intasome assembly and inhibition of DNA strand transfer. Nature 464: 232–236.
36. Hare S, Vos AM, Clayton RF, Thuring JW, Cummings MD, et al. (2010) Molecular mechanisms of retroviral integrase inhibition and the evolution of viral resistance. Proc Natl Acad Sci U S A 107: 20057–20062.
37. Boyd VA, Mason J, Hanumesh P, Price J, Russell CJ, et al. (2009) 2-Substituted-4,5-dihydroxypyrimidine-6-carboxamide antiviral targeted libraries. J Comb Chem 11: 1100–1104.
38. Kuzuhara T, Iwai Y, Takahashi H, Hatakeyama D, Echigo N (2009) Green tea catechins inhibit the endonuclease activity of influenza A virus RNA polymerase. PLoS Curr 1: RRN1052.
39. Song JM, Lee KH, Seong BL (2005) Antiviral effect of catechins in green tea on influenza virus. Antiviral Res 68: 66–74.
40. Baughman BM, Slavish PJ, Dubois RM, Boyd VA, White SW, et al. (2012) Identification of Influenza Endonuclease Inhibitors via a Novel Fluorescence Polarization Assay. ACS Chem Biol 7: 526–34.
41. Kirschberg TA, Balakrishnan M, Squires NH, Barnes T, Brendza KM, et al. (2009) RNase H active site inhibitors of human immunodeficiency virus type 1 reverse transcriptase: design, biochemical activity, and structural information. J Med Chem 52: 5781–5784.
42. Lansdon EB, Liu Q, Leavitt SA, Balakrishnan M, Perry JK, et al. (2011) Structural and binding analysis of pyrimidinol carboxylic acid and N-hydroxy quinazolinedione HIV-1 RNase H inhibitors. Antimicrob Agents Chemother 55: 2905–2915.
43. Freire E, Waksman G (2005) A Thermodynamic Guide to Affinity Optimization of Drug Candidates: Proteomics and Protein-Protein Interactions. Springer US. pp. 291–307.
44. Hamelberg D, McCammon JA (2004) Standard free energy of releasing a localized water molecule from the binding pockets of proteins: double-decoupling method. J Am Chem Soc 126: 7683–7689.
45. Michel J, Tirado-Rives J, Jorgensen WL (2009) Energetics of displacing water molecules from protein binding sites: consequences for ligand optimization. J Am Chem Soc 131: 15403–15411.
46. Lam PY, Jadhav PK, Eyermann CJ, Hodge CN, Ru Y, et al. (1994) Rational design of potent, bioavailable, nonpeptide cyclic ureas as HIV protease inhibitors. Science 263: 380–384.
47. Nowotny M, Gaidamakov SA, Crouch RJ, Yang W (2005) Crystal structures of RNase H bound to an RNA/DNA hybrid: substrate specificity and metal-dependent catalysis. Cell 121: 1005–1016.
48. Nowotny M, Yang W (2006) Stepwise analyses of metal ions in RNase H catalysis from substrate destabilization to product release. Embo J 25: 1924–1933.
49. Morin B, Coutard B, Lelke M, Ferron F, Kerber R, et al. (2010) The N-terminal domain of the arenavirus L protein is an RNA endonuclease essential in mRNA transcription. PLoS Pathog 6: e1001038.
50. Birch AJ, Salahud-Din M, Smith DCC (1966) The synthesis of (+/−)-xanthorrhoein. J Chem Soc C: Organic: 523–527.
51. Koch U, Attenni B, Malancona S, Colarusso S, Conte I, et al. (2006) 2-(2-Thienyl)-5,6-dihydroxy-4-carboxypyrimidines as inhibitors of the hepatitis C virus NS5B polymerase: discovery, SAR, modeling, and mutagenesis. J Med Chem 49: 1693–1705.
52. Otwinowski Z, Minor W, Charles W . Carter, Jr. (1997) Processing of X-ray diffraction data collected in oscillation mode. Methods Enzymol: Academic Press. pp. 307–326.
53. McCoy AJ, Grosse-Kunstleve RW, Storoni LC, Read RJ (2005) Likelihood-enhanced fast translation functions. Acta Crystallogr D Biol Crystallogr 61: 458–464.
54. Adams PD, Afonine PV, Bunkoczi G, Chen VB, Davis IW, et al. (2010) PHENIX: a comprehensive Python-based system for macromolecular structure solution. Acta Crystallogr D Biol Crystallogr 66: 213–221.
55. Emsley P, Cowtan K (2004) Coot: model-building tools for molecular graphics. Acta Crystallogr D Biol Crystallogr 60: 2126–2132.
56. Murshudov GN, Vagin AA, Dodson EJ (1997) Refinement of macromolecular structures by the maximum-likelihood method. Acta Crystallogr D Biol Crystallogr 53: 240–255.